

## Article

# Evolution of the Soot-Particle Size Distribution Function in the Cylinder and Exhaust System of Piston Engines: Simulation

Sergey M. Frolov <sup>1,2,\*</sup> , Konstantin A. Avdeev <sup>2</sup>, Vladislav S. Ivanov <sup>1,2</sup>, Pavel A. Vlasov <sup>2</sup> , Fedor S. Frolov <sup>1,2</sup>, Ilya V. Semenov <sup>1</sup> and Marina S. Belotserkovskaya <sup>1</sup>

<sup>1</sup> Department of Computational Mathematics, Federal State Institution “Scientific Research Institute for System Analysis of the Russian Academy of Sciences”, Moscow 117218, Russia

<sup>2</sup> Department of Combustion and Explosion, Semenov Federal Research Center for Chemical Physics of the Russian Academy of Sciences, Moscow 119991, Russia

\* Correspondence: smfrol@chph.ras.ru

**Abstract:** A computational tool for simulating the temporal evolution of the soot-particle size distribution function (SDF) in the internal combustion engine (ICE) and in the attached exhaust pipe is developed and tested against available experimental data on the soot-particle SDF at the outlet of the exhaust system. Firstly, a database of soot particle properties (particle mean diameter, dispersion, total particle number density vs. time for different fuels, fuel-to-air equivalence ratios, temperatures, pressures, and exhaust gas recirculation) is developed based on the thoroughly validated detailed model of soot formation under ICE conditions. The database is organized in the form of look-up tables. Secondly, the soot-particle SDF in the database is approximated using the log-normal SDF, which is directly used in the multidimensional calculations of the ICE operation process. Thirdly, the coagulation model of soot particles is developed, which includes three coagulation mechanisms: Brownian, turbulent-kinetic, and turbulent-diffusion. This model is applied for simulating the evolution of the soot-particle SDF in the exhaust pipe after opening the exhaust valve. Calculations show that the coagulation process of soot particles in the exhaust pipe has a significant effect on the mean size of particles at the outlet of the exhaust system (the mean particle diameter can increase by almost an order of magnitude), and the dominant mechanism of particle coagulation in the exhaust system of a diesel engine is the Brownian mechanism. The objective, approach, and obtained results are the novel features of the study.

**Keywords:** reciprocating engine; soot particles; size distribution function; number density; exhaust manifold; particle coagulation; temporal evolution of size distribution function



**Citation:** Frolov, S.M.; Avdeev, K.A.; Ivanov, V.S.; Vlasov, P.A.; Frolov, F.S.; Semenov, I.V.; Belotserkovskaya, M.S. Evolution of the Soot-Particle Size Distribution Function in the Cylinder and Exhaust System of Piston Engines: Simulation. *Atmosphere* **2023**, *14*, 13. <https://doi.org/10.3390/atmos14010013>

Academic Editor: Xin Wang

Received: 22 November 2022

Revised: 14 December 2022

Accepted: 19 December 2022

Published: 22 December 2022



**Copyright:** © 2022 by the authors. Licensee MDPI, Basel, Switzerland. This article is an open access article distributed under the terms and conditions of the Creative Commons Attribution (CC BY) license (<https://creativecommons.org/licenses/by/4.0/>).

## 1. Introduction

The European environmental standard Euro-VI limits both the content of smoke/soot particles (less than 5 mg/km) and their number density (less than  $6 \times 10^{11} \text{ (km)}^{-1}$ ) in the exhaust gases of internal combustion engines (ICEs) [1]. Such stringent limitations lead to the need for further improvement of the ICE operation process, as well as the use of special exhaust gas cleaning systems in the design of ICEs such as particulate filters installed in the exhaust pipe. In the exhaust gases of ICEs, the condensed phase is primarily represented using soot particles with adsorbed volatile organic compounds and polycyclic aromatic hydrocarbons (PAHs), as well as inorganic sulfur- and nitrogen-containing compounds and, to a lesser extent, microdroplets of the condensate of volatile organic compounds and inorganic compounds. Therefore, in view of the current limitations, ICE developers are working, on the one hand, to further improve the operation process to significantly reduce soot emissions, and, on the other hand, to further improve the design of filters, converters, and particle afterburners in the engine exhaust system.

Improving the operation process in ICEs is impossible without a deep understanding of all the physical and chemical processes accompanying smoke/soot formation in the

engine cylinder. This requires models that are capable of predicting not only the soot yield in the processes of pyrolysis, oxidation, and combustion but also the size distribution function (SDF) of soot particles both in the engine cylinder and exhaust manifolds [2–5]. The development of such models is a very difficult task since its solution requires a detailed simulation of the process of soot formation in an ICE cylinder with a description of the various mechanisms for the appearance of nuclei, their growth, and the shape and structure of clusters, as well as the various chemical processes with their participation, including homogeneous and heterogeneous reactions. A detailed model of soot formation (DMS) during pyrolysis and partial oxidation of hydrocarbons has been under development at the SFC for a long time. This model has been implemented in the MACRON code [6–8]. The basis of this model is a detailed chemical reaction scheme for the calculation of soot formation and oxidation. It combines the mechanisms of formation of PAHs, polyynes, mechanisms of soot precursor formation due to condensation of polyaromatic and polyynes molecules, soot particle growth using the reactions of HACA (H-abstraction-Acetylene-addition) mechanism and polyynes molecule addition, the mechanism of acetylene pyrolysis and pure carbon cluster formation, and the reactions of hydrocarbon (up to n-hexadecane) oxidation [9–14]. The most important advantage of this model is that it satisfactorily describes all the available experimental data on the soot yield during pyrolysis and partial oxidation of various hydrocarbons obtained in kinetic shock tubes. Its other advantage is that it operates with characteristics of the condensed phase such as the particle number density, particle diameter, mean particle diameter, and particle SDF. The noted advantages allow one to consider this model as a tool for solving the above problem, given that is determining the number and the size of soot particles in the cylinder and in the exhaust gases of ICEs.

At present, the development of detailed kinetic models of soot formation continues. The recent work of Frenklach and Mebel should be noted [15], in which all existing approaches to the description of the formation of soot particle nuclei are analyzed in great detail, taking into account their possible structure, lifetime, as well as kinetic and thermodynamic aspects. In his pioneering work on detailed kinetic modeling of the soot formation process [16], Frenklach proposed the HACA mechanism to explain the rapid growth of polyaromatic hydrocarbons, and then the surface growth of the soot particles themselves. The main role in this mechanism is played by the activation of a growing hydrocarbon fragment due to the abstraction of a hydrogen atom and the formation of an active site to which an acetylene molecule can be attached, introducing two carbon atoms into the growing fragment. Consideration of the structural limitations when attaching an acetylene molecule shows that a five-membered ring of carbon atoms is formed, which can then turn into a six-membered ring. Numerous computational and experimental works have confirmed the main consequences of the HACA mechanism. Further development of the HACA mechanism led to an understanding that the activation process of a reacting particle can occur not only by splitting off the hydrogen atom but also when it is attached and even when a hydrogen atom migrates inside the particle. As a monomer for the primary act of the process of formation of soot particle nuclei, Frenklach proposed the process of physical condensation of two pyrene molecules consisting of four fused aromatic rings. However, the Van der Waals attraction forces for pyrene molecules are too weak for the resulting dimer to survive until the next collision. The concept of rotational excitation of one of the fragments was proposed, which was supposed to stabilize the resulting complex. Currently, the hypothesis of the bridge-forming reactions of a dimer formation is more popular.

The defining role of polyaromatic structures in the formation of soot particle nuclei is confirmed using experiments with high-resolution atomic force microscopy (AFM) [17]. Aromatic structures with one, two, three, or more aromatic rings, structures with five-membered rings and aliphatic side chains, as well as linear polyynes-like structures were experimentally determined (Figure 1).

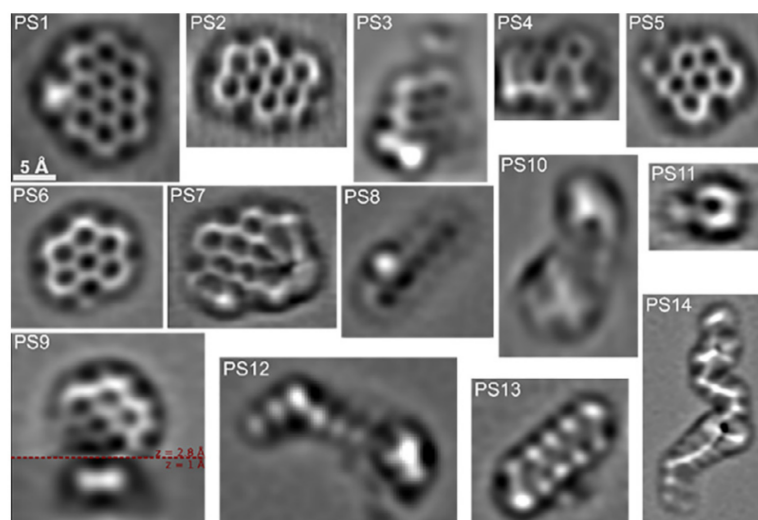


**Figure 1.** Laplacian-filtered AFM images of identified PAH molecules and aliphatic chains/substituted benzenes found in the soot particles collected at  $Z = 14$  mm burner-to-probe separation distance (primary soot particles) [17]. All images from PS1 to PS14 have the same scale.

The formation of PAHs according to the sequence of HACA reactions is accompanied by the formation of five-membered rings. To date, experimental studies have established the presence of five-membered aromatic rings in the PAH precursors of soot nuclei and young soot particles [18,19].

A very important issue is the question of the participation of smaller aromatic structures even with one or two aromatic rings in the process of the formation of soot nuclei. Recently, several researchers have given a positive answer to this question [20,21]. However, there is no definite answer to the question of how the formation of the nuclei of soot particles begins and how this process further proceeds.

Therefore, one is faced with a dilemma. On the one hand, existing theoretical knowledge cannot fully explain the occurrence of soot particles. On the other hand, numerical modeling of flames, apparently requires that, in order to correspond to the experimentally observed moment of the appearance of soot particles, the initiating PAH should be the size of a pyrene, and dimerization would be considered as an irreversible process, possibly with a rate reduced by no more than an order of magnitude [22]. In addition, one cannot fully explain the apparent irreversibility of such a process. Moreover, experiments in shock tubes, when the reaction time is limited to several milliseconds, convincingly indicate that much smaller molecular fragments with one or two aromatic rings should participate in the formation of soot particle nuclei.

In the DMS, the nuclei of soot particles are formed in the processes involving a stable polyaromatic molecule and a radical, or two radicals, although the contribution of purely radical reactions is very small. In the case of pyrolysis of acetylene and ethylene, when the concentration of PAHs is relatively low compared with pyrolysis and oxidation of other hydrocarbons, the nuclei of soot particles in the DMS are formed from polyynelike fragments. Thus, depending on the specific hydrocarbon, either the polyaromatic or polyynelike pathways of soot nuclei formation dominate in the model.

Speaking about the soot-particle size distribution function, it should be emphasized that bimodal functions are very often represented in the literature. Bimodality will also appear in the DMS if one takes into account the nuclei of soot particles and not just only soot particles. The boundary between them in the DMS is still conditional, but in the future, with further improvement of the model and the appearance of an increasing number of experimental data on the bimodality of the particle SDF, it would be possible to clarify these boundaries, which will probably also clarify the situation of what is considered as a nucleus of soot particle and what is a mature soot particle.

At long times, simultaneously with the coagulation process, there is a process of physical aggregation (adhesion) of primary spherical soot particles. Secondary soot particles with a certain fractal dimension are formed. The formal determination of the size of such particles is still a difficult task.

To design filters, converters, and particle afterburners, there is a need for information on the evolution of the SDF of smoke/soot particles during the motion of the turbulent flow of exhaust gases through the manifolds of the exhaust system. Since the measurements of exhaust emissions are taken at the outlet of the exhaust system, this will help solve the important inverse problem, i.e., determine the true particle SDF in the engine cylinder. It is known [23,24] that one of the reasons for changing the parameters of particle SDFs is their coagulation. In turbulent flows with ultrafine particles (submicron and nanometer sizes) under conditions of relatively low temperatures, coagulation occurs mainly in accordance with three mechanisms [23–27]: Brownian, turbulent–kinetic, and turbulent–diffusion. It is expected that the Brownian mechanism dominates for particles whose size is commensurate with the size of the molecules of the carrier medium [23,24]. The turbulent–kinetic mechanism takes into account that the complete entrainment of particles by turbulent pulsations does not occur, and a difference can be observed between the velocities of the particles and the carrier medium. In this case, particle coagulation is caused by inertial effects. The turbulent–diffusion mechanism is caused by the fact that the particles are carried away by turbulent velocity fluctuations, which lead to their collisions and coagulation. The complex nature of the gas flows in ICE exhaust systems makes it impossible to give preference to any of these mechanisms. A situation is likely where the dominant coagulation mechanism changes along the length of the exhaust system.

This manuscript is aimed at the development of a computational tool allowing for simulating the soot-particle SDF at the entrance to the ICE exhaust pipe and further temporal evolution of this SDF due to particle coagulation involving all the main mechanisms: Brownian, turbulent–kinetic, and turbulent–diffusion. This objective, approach, and the obtained results are the novel features of the manuscript.

## 2. Materials and Methods

### 2.1. Flow Simulation in the Engine Cylinder and Exhaust System

The object of this investigation is a diesel engine of a passenger car with a common-rail injector. The engine operation mode includes: the crankshaft speed is  $n = 3000 \text{ min}^{-1}$ ; the maximum droplet velocity in the fuel spray is 577 m/s; the initial temperature of fuel droplets in the spray is  $T_{d0} = 330 \text{ K}$ ; the overall fuel-to-air equivalence ratio is  $\Phi = 0.52$ ; and the mass fraction of exhaust gas in the fuel–air mixture (Exhaust Gas Recirculation) is  $\text{EGR} = 0$ . The fuel is n-tetradecane. It is shown in [28] that n-tetradecane can be used as a surrogate for diesel oil. Figure 2 shows the geometry of the computational domain. The moving computational mesh is used. The mesh dependence on the computational results is checked by reducing the mean cell size by a factor of approximately 2. A calculation starts when the intake valve closes ( $35^\circ$  crank angle (CA) after the bottom dead center (BDC)) and ends when the exhaust valve is opened ( $40^\circ$  CA before the BDC). The initial rotation of the intake air is specified using the rotation law of the solid body. Fuel injection starts at  $701.8^\circ$  CA. The calculations are made using AVL FIRE<sup>®</sup> v2014 code [29] and are based on the RANS (Reynolds-averaged Navier–Stokes) equations. The  $k - \xi - f$  turbulence model is used for turbulence closure [30]. In the quasi-laminar combustion model, each computational cell is treated as a perfectly stirred reactor with the use of the detailed kinetic mechanism of fuel oxidation. For decreasing the computational cost, the multizone approach algorithm available in the code is used. To calculate the motion, evaporation, and break-up of liquid fuel droplets, the standard Lagrangian-droplet method is applied. The initial diameter of the droplets is assumed to be equal to the nozzle diameter ( $120 \mu\text{m}$ ). For soot modeling, the kinetic soot model available in the code is used (see Appendix A). Figure 3 shows a 3D computational mesh of the ICE exhaust system, including a pipe with a total length of 1.3 m and variable diameter. The diameter of the pipe inlet and outlet

sections is 73 mm. The mean-flow equations are solved in Cartesian coordinates  $(x, y, z)$  using the collocated arrangement of variables.

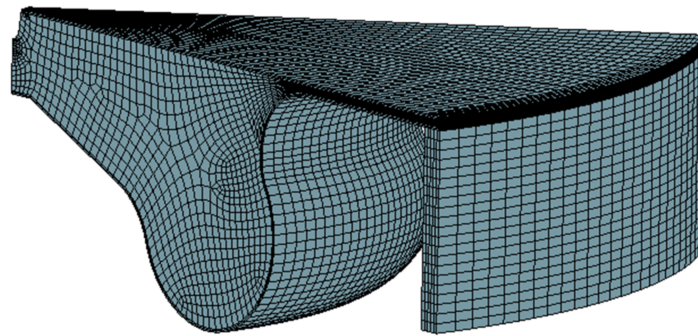


**Figure 2.** Geometry of the computational domain at the top dead center of the ICE.

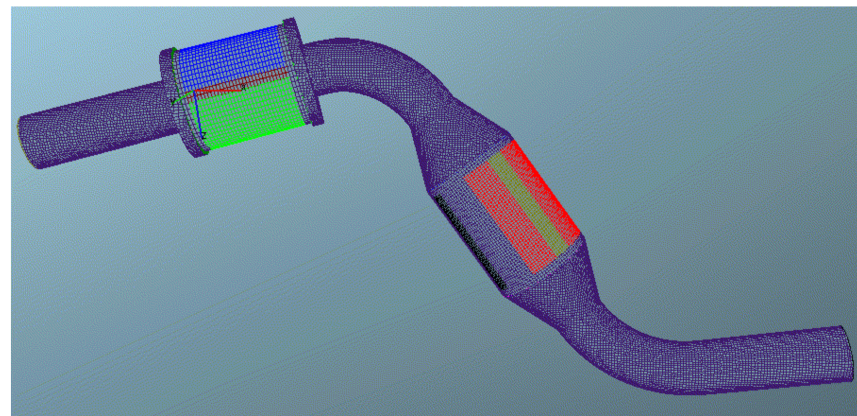


**Figure 3.** The computational mesh of the ICE exhaust system.

The AVL FIRE<sup>®</sup> code solves the general conservation law written in the integral form for the control volume with the outward surface vectors,  $\vec{A} = A_k \vec{i}_k$ :

$$\frac{d}{dt} \int_V \rho \phi dV + \iint_A \rho \phi U_k dA_k = \iint_A \Gamma_{\phi}^{kk} \frac{\partial \phi}{\partial x_k} dA_k + \int_V S_{\phi}^V dV + \iint_A S_{\phi k}^A dA_k \quad (1)$$

where a variable  $\phi(x_k, t)$  represents either a scalar or vector and the tensor field components, and tensor notation is employed;  $t$  is time;  $\rho$  is the density;  $U_k$  is the velocity vector components;  $\Gamma_{\phi}^{kk}$  is the diffusion coefficient for the variable  $\phi$ ; and  $S_{\phi}^V$  and  $S_{\phi k}^A$  are the volumetric and surface source terms, respectively. The terms in Equation (1) correspond to the rate of change,  $R$  (first term), convection,  $C$  (second term), diffusion,  $D$  (third term), and sources,  $S$  (fourth and fifth terms).

For a typical computational cell  $P$  with the volume  $V$  surrounded by its neighbors  $P_j$ , the discretized control volume equation is written as:

$$\frac{d}{dt} (\rho_P V_P \phi_P) + \sum_{j=1}^{n_f} C_j - \sum_{j=1}^{n_f} D_j = (S_{\phi}^V)_P V_P + \sum_{j=1}^{n_f} (S_{\phi k}^A A_k)_j \quad (2)$$

where  $C_j$  and  $D_j$  are convective and diffusion transport through the face  $j$ , respectively; and  $n_f$  is the number of cell faces. In the code, the first term in Equation (1) is discretized using two implicit schemes, namely the first-order accurate Euler (two-time-level) scheme and

the second-order accurate three-time-level scheme [31]. A deferred correction approach is used for treatment of convection fluxes:

$$C_j = \dot{m}_j \phi_j^{UPWIND} + \underline{\gamma_\phi |\dot{m}_j| \varphi_j (\phi_{P_j} - \phi_P)} \tag{3}$$

where  $\dot{m}_j = \rho \vec{U}_j \cdot \vec{A}_j$  is the mass flux and  $\gamma_\phi$  is the blending factor between UPWIND and the higher-order scheme ( $0 \leq \gamma \leq 1$ ). The underlined term is calculated by using values from the previous iteration step. The flux limiter,  $\varphi_j$ , is provided using the higher-order differencing scheme and to ensure a bounded solution, as described in [32]. The diffusion term is discretized using the approach [33]:

$$D_j = \bar{\Gamma}_{\phi_j} \frac{\vec{A}_j \cdot \vec{A}_j}{d_j \cdot A_j} (\phi_{P_j} - \phi_{P_0}) + \bar{\Gamma}_{\phi_j} \left( \frac{\vec{\nabla} \phi_j \cdot \vec{A}_j - \frac{\vec{A}_j \cdot \vec{A}_j}{A_j \cdot d_j} \vec{\nabla} \phi_j \cdot \vec{d}_j}{\vec{\nabla} \phi_j \cdot \vec{A}_j - \frac{\vec{A}_j \cdot \vec{A}_j}{A_j \cdot d_j} \vec{\nabla} \phi_j \cdot \vec{d}_j} \right) \tag{4}$$

Cell gradients are calculated by using either the Gauss' theorem, thus:

$$\nabla \phi_P = \frac{1}{V_P} \sum_{j=1}^{n_f} \phi_j \vec{A}_j \tag{5}$$

or a linear least-square approach [34]. This diffusion model removes unphysical oscillations. The outcome of the discretization above is a set of algebraic equations: one for each control volume and for each transport equation. An algebraic equation can be written as:

$$a_P \phi_P = \sum_{j=1}^{n_f} a_j \phi_{P_j} + S_\phi \tag{6}$$

where  $a_p$  and  $a_j$  are coefficients and  $S_\phi$  is the source term. For the solution of a linear set of equations, a conjugate gradient (CG) type of solver and an algebraic multi-grid (AMG) are used [35] (AMG is used by default for the pressure and CG for all other equations). The overall solution procedure is iterative and is based on the SIMPLE algorithm [36].

### 2.2. Simulation of Soot Formation Using MACRON Code

In this section, we briefly describe the theoretical background for simulating the soot-particle SDF in the MACRON code [7] and outline the procedure which is used for construction of the SDF. The classical statistical moments of a given distribution density function  $P_s(t)$  are defined as:

$$\mu_k(t) = \sum_{s=1}^{\infty} s^k P_s(t) \quad k = 0, 1, \dots \tag{7}$$

where  $s$  is the number of carbon atoms in the soot cluster. Insertion of this definition into the kinetic model leads to a system of ordinary differential equations for the statistical moments  $\mu_0, \mu_1, \dots$ , etc. The (bounded) infinite sequence  $\mu_0, \mu_1, \dots$ , determines the distribution density function  $P_s(t)$ , which is the well-known Stieltjes problem in mathematical statistics. If, however, only a finite number of moments  $\mu_0, \mu_1, \dots, \mu_n$  is known, then the associated approximations,  $P_s^{(n)}$ , of the  $P_s$  may vary within an extremely wide range.

The method used in the MACRON code aims, on the one hand, at preserving the advantages of both the statistical moment treatment and the continuous Galerkin method and, on the other hand, at avoiding the intrinsic disadvantages of both approaches. The starting point is the fact that the number of carbon atoms in the soot cluster,  $s$ , is a discrete variable. The key to the construction of the basic scheme is the introduction of a discrete inner product:

$$(f, g) = \sum_{s=1}^{\infty} f(s)g(s)\Psi(s) \tag{8}$$

where  $\Psi$  is a weight function with  $\Psi(s) > 0, s = 1, 2, \dots < \Gamma$  characterizing the inner product  $(f, g)$ . This inner product induces the norm:

$$\|f\|_{\Psi} = (f, f)^{1/2} \tag{9}$$

and the associated Hilbert space,  $H_{\Psi}$ . Under the necessary and sufficient condition:

$$v_k = \sum_{s=1}^{\infty} s^k \Psi(s) < \infty \quad k = 0, 1, \dots \tag{10}$$

$H_{\Psi}$  has an orthogonal polynomial basis  $\{l_j(s)\}_{j=0,1,\dots}$  satisfying the condition:

$$(l_i, l_j) = g_i \delta_{ij}, \quad g_i > 0, \quad i, j = 0, 1, 2, \dots \tag{11}$$

where  $\delta_{ij}$  is the Kronecker delta. Assume that:

$$\overline{P_s(t)} = \frac{P_s(t)}{\Psi(s)} \in H_{\Psi} \tag{12}$$

Then, there exists a unique representation:

$$P_s(t) = \Psi(s) \sum_{k=0}^{\infty} a_k(t) l_k(s) \tag{13}$$

Appropriate treatment of the kinetic equations using the above formalism leads to a system of ordinary differential equations for the generalized moments. Truncation of the expansion after  $n$  terms leads to the Galerkin approximation:

$$P_s^{(n)}(t) = \Psi(s) \sum_{k=0}^n a_k^{(n)}(t) l_k(s) \tag{14}$$

The Galerkin approximation is used in the MACRON code to calculate the temporal evolution of soot particle size distribution. In addition to the size distribution, the MACRON code calculates the following time-dependent mean variables:

- Mean particle diameter  $\bar{d} = \mu_1 / \mu_0$ ;
- Mean particle mass  $\bar{m} = \mu_2 / \mu_1$ ;
- Variance  $\delta = \bar{m} / \bar{d} = \mu_0 \mu_2 / \mu_1^2$ .

One can approximate the particle SDF using the log-normal law:

$$\text{SDF}(t) = \frac{n_{\Sigma}}{\sqrt{2\pi}d\sigma} \exp \left[ -\frac{\ln^2(d/\bar{d})}{2\sigma^2} \right] \tag{15}$$

where  $d(t)$  is the particle diameter,  $\sigma(t) = \sqrt{\ln(\delta)}$  (dispersion), and  $n_{\Sigma}(t)$  is the total particle number density per unit volume, determined as the integral:

$$n_{\Sigma} = \int_{d_{\min}}^{d_{\max}} \text{SDF}(z) dz \tag{16}$$

with  $d_{\min}$  and  $d_{\max}$  being the minimum and maximum particle diameter. As seen, the SDF depends on three parameters  $n_{\Sigma}(t), \bar{d}(t)$ , and  $\sigma(t)$ , which can be taken from the MACRON code calculations. Multiple examples presented in [7] indicate that the log-normal SDF of Equation (15) approximates well the detailed calculations made using the MACRON code.

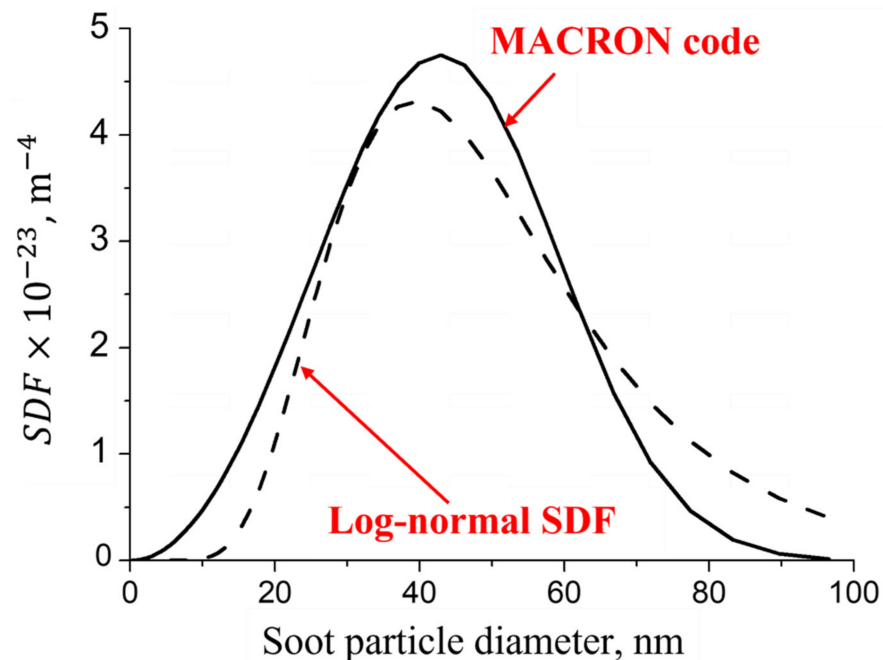
### 2.3. Database for Soot-Particle SDF

Based on the DMS, a database for simulating the approximate log-normal SDF (15) of soot particles in relation to ICEs was developed. The database is formatted in the form of look-up tables and can be used in multidimensional calculations of the ICE operation process. Given below is a brief description of the database. Table 1 shows a list of conditions for which soot formation calculations were conducted. The notations adopted in the table are as follows:  $T$  is the temperature,  $p$  is the pressure,  $\Phi$  is the fuel-to-air equivalence ratio, EGR is the mass fraction of exhaust gas in the mixture (Exhaust Gas Recirculation parameter), and  $\tau$  is the process time. It should be noted that, at a lower temperature limit of 1300–1400 K, almost no soot was detected in the MACRON code calculations during a process time of  $0 \leq \tau \leq 3$  ms, and at an upper limit of 2400–2800 K, all the formed soot was oxidized.

**Table 1.** The list of conditions included in the database.

Fuel	$T$ , K	$p$ , atm	$\Phi$	EGR	$\tau$ , ms										
CH <sub>4</sub>	1300–2700	1–240	2–4	0.0–0.6	0–3										
C <sub>2</sub> H <sub>5</sub> OH	1400–2600	1–240	2–4	0.0–0.6	0–3										
C <sub>3</sub> H <sub>8</sub>	1300–2800	1–240	2–4	0.0–0.6	0–3										
n-C <sub>7</sub> H <sub>16</sub>	1300–2800	1–240	2–4	0.0–0.6	0–3										
i-C <sub>8</sub> H <sub>18</sub>	1300–2400	1–240	2–4 </tr <tr> <td>n-C<sub>10</sub>H<sub>22</sub></td> <td>1300–2700</td> <td>1–240</td> <td>2–4</td> <td>0.0–0.6</td> <td>0–3</td> </tr> <tr> <td>n-C<sub>14</sub>H<sub>30</sub></td> <td>1300–2800</td> <td>1–240</td> <td>2–4</td> <td>0.0–0.6</td> <td>0–3</td> </tr>	n-C <sub>10</sub> H <sub>22</sub>	1300–2700	1–240	2–4	0.0–0.6	0–3	n-C <sub>14</sub> H <sub>30</sub>	1300–2800	1–240	2–4	0.0–0.6	0–3
n-C <sub>10</sub> H <sub>22</sub>	1300–2700	1–240	2–4	0.0–0.6	0–3										
n-C <sub>14</sub> H <sub>30</sub>	1300–2800	1–240	2–4	0.0–0.6	0–3										

Figure 4 compares the approximate log-normal soot-particle SDF of Equation (15) with the results of direct calculations using the MACRON code for a fuel-rich n-tetradecane–air mixture at  $\Phi = 4$ ,  $p = 100$  atm,  $T = 2200$  K, EGR = 0.6, and  $\tau = 3.0$  ms. It can be seen that the approximation of Equation (15) is satisfactory.



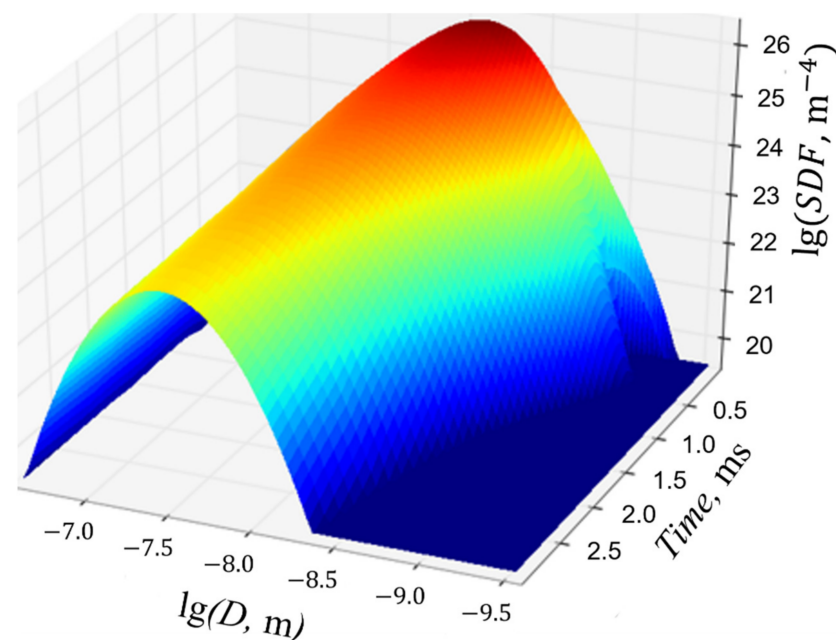
**Figure 4.** Illustration of the approximation accuracy of the soot-particle SDF obtained using MACRON code calculation with the log-normal SDF of Equation (15). Fuel: n-C<sub>14</sub>H<sub>30</sub>,  $\Phi = 4$ ,  $p = 100$  atm,  $T = 2200$  K, EGR = 0.6, and  $\tau = 3.0$  ms.

Table 2 shows a fragment of the look-up table for the three parameters ( $n_{\Sigma}$ ,  $\bar{d}$ , and  $\sigma$ ) of the soot-particle log-normal SDF for the methane–air mixture diluted with exhaust

gas (EGR = 0.2) at  $\Phi = 2$ ,  $p = 180$  atm, and  $T = 1700$  K. In addition, Figure 5 shows the temporal evolution of the log-normal SDF for the n-heptane–air mixture at  $\Phi = 4$ ,  $p = 10$  atm,  $T = 2000$  K, and EGR = 0. When plotting Figure 5, the corresponding look-up table from the database was used. It can be seen that for the conditions of Figure 5, the mean diameter of soot particles increases with time, reaching 40.8 nm. Figure 6 demonstrates how the log-normal SDF of Equation (15) approximates the soot-particle SDF predicted using the MACRON code for n-tetradecane fuel with EGR = 0.6 at some  $\Phi - p - T$  conditions and time instants from  $\sim 0.1$  to 3.0 ms. As was mentioned earlier in this paper, the most important advantage of the MACRON code is that it satisfactorily describes all the available experimental data on the soot yield during pyrolysis and partial oxidation of various hydrocarbons. In view of this, the fact that the log-normal SDF of Equation (15) approximates satisfactorily the soot-particle SDF predicted using the MACRON code can be treated as verification of simulation model accuracy.

**Table 2.** A fragment of the look-up table for the parameters of the log-normal SDF of soot particles (fuel: CH<sub>4</sub>,  $\Phi = 2$ ;  $p = 180$  atm;  $T = 1700$  K, EGR = 0.2,  $0 \leq \tau \leq 3$  ms).

Time, ms	$n_{\Sigma}, \text{m}^{-3}$	$\bar{d}, \text{nm}$	$\sigma$
0.0	0.0	3.72	0.000
0.5	$3.2 \times 10^{19}$	9.87	0.417
1.0	$4.5 \times 10^{19}$	14.0	0.609
1.5	$3.9 \times 10^{19}$	16.5	0.693
2.0	$3.4 \times 10^{19}$	18.5	0.740
2.5	$3.0 \times 10^{19}$	19.9	0.765
3.0	$2.6 \times 10^{19}$	21.4	0.785



**Figure 5.** Time evolution of the soot-particle log-normal SDF for the n-heptane–air mixture at  $\Phi = 4$ ,  $p = 10$  atm,  $T = 2000$  K, and EGR = 0.

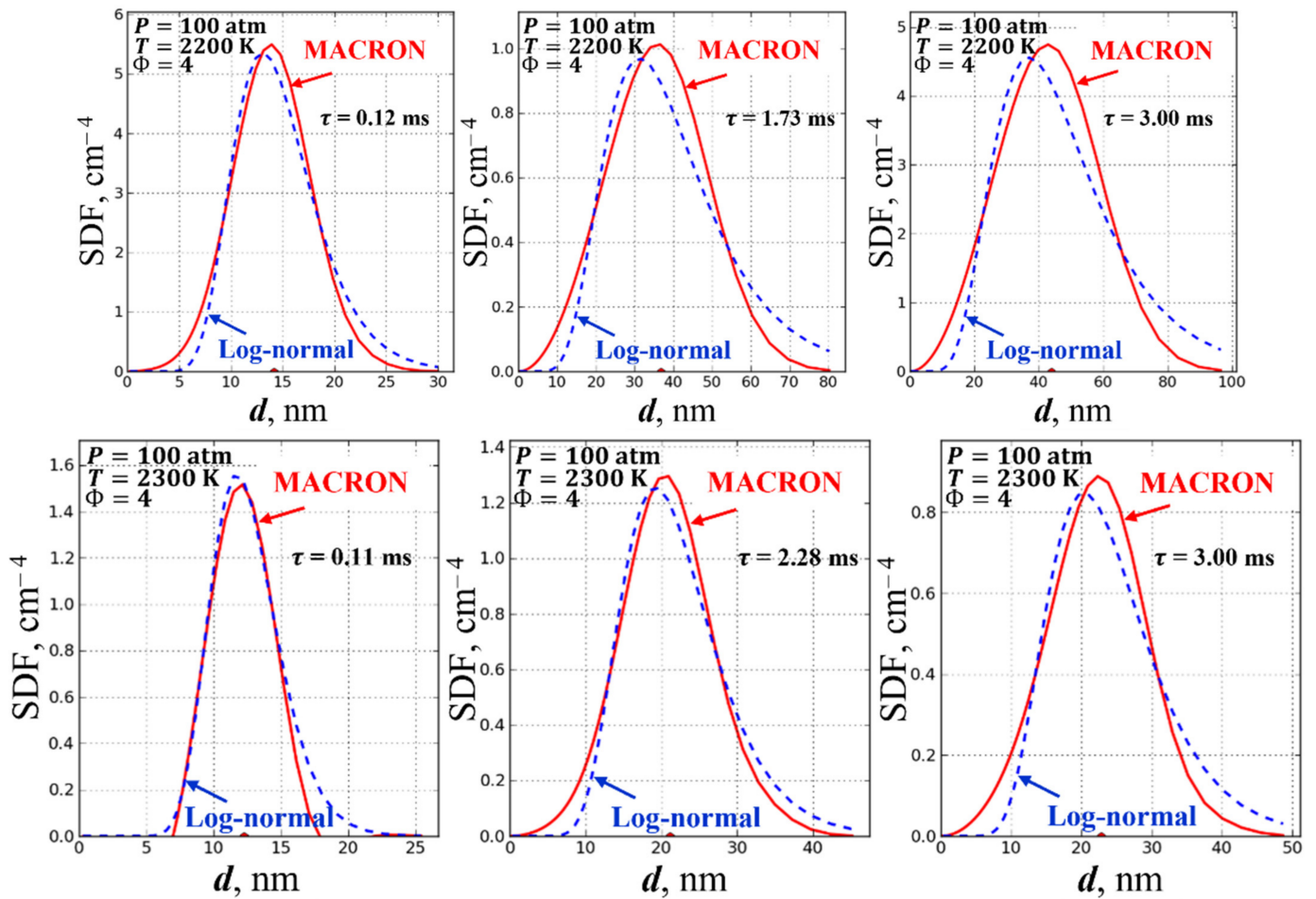


**Figure 6.** The soot-particle SDF predicted using the MACRON code and its log-normal approximation for n-tetradecane fuel with EGR = 0.6 at some  $\Phi - p - T$  conditions and time instants from ~0.1 to 3.0 ms.

#### 2.4. Model of Soot Particle Coagulation in the Engine Exhaust System

The model of soot particle coagulation in the ICE exhaust system is based on several simplifying assumptions:

- The gas flow in the exhaust system is one-dimensional, quasi-stationary, and is known a priori;
- The soot-particle velocity does not differ from the average gas velocity;
- The soot-particle size changes only due to coagulation;
- The coagulation probability of soot particles of different sizes during collisions is 1;
- The coagulation probability of identical soot particles in collisions is 0;
- The initial soot-particle SDF is described using the log-normal SDF of Equation (15):

$$SDF_{in} = \frac{n_{\Sigma,in}}{\sqrt{2\pi}d\sigma_{in}} \exp\left[-\frac{\ln^2(d/d_{in})}{2\sigma_{in}^2}\right] \quad (17)$$

where parameters  $n_{\Sigma,in}$ ,  $d_{in}$ , and  $\sigma_{in}$  are the soot-particle number density, mean diameter, and dispersion in the initial log-normal distribution function at the inlet to the ICE exhaust system, respectively.

These assumptions allow one to write the following equation for the number density of soot particles,  $n_{\Sigma}$ :

$$\frac{dn_{\Sigma}}{dx} = \frac{1}{V_g(x)} \left(\frac{dn_{\Sigma}}{dt}\right)_{coag} \quad (18)$$

where  $x$  is the longitudinal coordinate,  $V_g$  is the gas velocity, and the differential term in the right-hand side of Equation (18) is the rate of particle coagulation [23]:

$$\left(\frac{dn_\Sigma}{dt}\right)_{coag} = - \int_0^\infty n(d_2) \left\{ \int_0^{d_2} \beta(d_1, d_2) n(d_1) dd_1 \right\} dd_2 \tag{19}$$

Here,  $n(d)dd$  is the number density of soot particles with an equivalent diameter ranging from  $d$  to  $d + dd$ ,  $\beta(d_1, d_2) = \beta_B(d_1, d_2) + \beta_{tk}(d_1, d_2) + \beta_{td}(d_1, d_2)$  is the coagulation kernel (collision frequency) for soot particles with an equivalent diameter  $d_1$  and  $d_2$ , respectively, whereas the terms  $\beta_B(d_1, d_2)$ ,  $\beta_{tk}(d_1, d_2)$  and  $\beta_{td}(d_1, d_2)$  are the coagulation kernels for the Brownian, turbulent-kinetic, and turbulent-diffusion mechanisms, respectively, determined using the known relations given below [23–27].

#### 2.4.1. Brownian Coagulation

The coagulation kernel  $\beta_B(d_1, d_2)$  is defined as [25]:

$$\beta_B(d_1, d_2) = K_B(d_1, d_2) \left[ 1 + \text{Kn}(d_1, d_2) \frac{\zeta + \zeta \frac{K_B(d_1, d_2)}{K_{fm}(d_1, d_2)}}{1 + \zeta \text{Kn}(d_1, d_2)} \right]^{-1} \tag{20}$$

where  $K_B$  is the coagulation coefficient:

$$K_B(d_1, d_2) = 2\pi(d_1 + d_2)(D_{B1} + D_{B2}) \tag{21}$$

$\text{Kn}$  is the Knudsen number:

$$\text{Kn}(d_1, d_2) = \frac{2\lambda_{12}}{(d_1 + d_2)} \tag{22}$$

$K_{fm}$  is the coagulation coefficient for the free-molecular mode, when the particle size is much less than the free path:

$$K_{fm}(d_1, d_2) = \left[ \frac{8\pi k_B T_g(x)(m_1 + m_2)}{m_1 m_2} \right]^{1/2} \frac{(d_1 + d_2)^2}{4} \tag{23}$$

$\zeta = 1.0161$  and  $\zeta = 4/3$  are the numerical factors;  $\lambda_{12}$  is the relative free path [ $m$ ]:

$$\lambda_{12} = \lambda_1 \sqrt{\frac{m_2}{m_1 + m_2}} + \lambda_2 \sqrt{\frac{m_1}{m_1 + m_2}} \tag{24}$$

$m_1$  and  $m_2$  are the masses of particles (kg);  $\lambda_1$  and  $\lambda_2$  are the effective particle free paths [ $m$ ]:

$$\lambda_1 = \frac{3D_{B1}}{\left(\frac{8k_B T_g(x)}{\pi m_1}\right)^{1/2}}; \lambda_2 = \frac{3D_{B2}}{\left(\frac{8k_B T_g(x)}{\pi m_2}\right)^{1/2}} \tag{25}$$

$k_B = 1.380650424 \cdot 10^{-23}$  J/kg is the Boltzmann constant;  $T_g(x)$  is the local gas temperature in the exhaust pipe (K);  $D_{B1}$  and  $D_{B2}$  are the diffusion coefficients ( $m^2/s$ ):

$$D_{B1} = \frac{1}{3\pi} \frac{k_B T_g(x) C_1}{\eta_g d_1} \text{ and } D_{B2} = \frac{1}{3\pi} \frac{k_B T_g(x) C_2}{\eta_g d_2} \tag{26}$$

$C_1$  and  $C_2$  are the Cunningham correction factors:

$$C_1 = 1 + \frac{2\lambda_m}{d_1} \left[ A + Q \exp\left(-\frac{ad_1}{2\lambda_m}\right) \right], C_2 = 1 + \frac{2\lambda_m}{d_2} \left[ A + Q \exp\left(-\frac{ad_2}{2\lambda_m}\right) \right] \tag{27}$$

$\eta_g$  is the dynamic gas viscosity (kg/m/s);  $\lambda_m$  is the mean free path of gas molecules (m):

$$\lambda_m = \frac{1}{\sqrt{2}\pi} \frac{k_B T_g(x)}{\rho_g(x) d_g^2} \tag{28}$$

$a = 1.1$ ,  $A = 1.257$ , and  $Q = 0.4$  are the coefficients,  $d_g \approx 0.28 \cdot 10^{-9}$  m is the mean diameter of gas molecules, and  $p_g(x)$  is the gas pressure (Pa).

#### 2.4.2. Turbulent–Kinetic Coagulation

Coagulation of particles possessing a density much higher than the gas density occurs as a rule via the turbulent–kinetic coagulation mechanism. Due to the density difference, particles are not completely involved into motion by turbulent gas vortices. Particles of different sizes move locally with different velocities. This is the reason why such particles collide with each other. To determine the coagulation kernel, one must know the velocity difference between particles. This difference is given using the relationship [24]:

$$\overline{(V_1 - V_2)^2} = (\tau_1^{-1} - \tau_2^{-1}) \overline{\left(\frac{du_g}{dt}\right)^2} \tag{29}$$

where  $\tau_1$  and  $\tau_2$  are the characteristic relaxation times of particle velocity and  $\overline{\left(\frac{du_g}{dt}\right)^2}$  is the mean value of the squared acceleration of pulsating gas velocity. It is known [24] that for the isotropic turbulence  $\overline{\left(\frac{du_g}{dt}\right)^2} \sim \frac{\varepsilon_D^{3/2}}{\nu_g^{1/2}}$ . Then Equation (29) can be rewritten in the form:

$$\overline{(V_1 - V_2)^2} = (\tau_1^{-1} - \tau_2^{-1}) \frac{\varepsilon_D^{3/2}}{\nu_g^{1/2}} \tag{30}$$

Using Equation (30), the authors of [9] derived the equation for the coagulation kernel:

$$\beta_{tk}(d_1, d_2) = 5.7 \left(\frac{d_1}{2} + \frac{d_2}{2}\right)^2 \left| \tau_1^{-1} - \tau_2^{-1} \right| \frac{\varepsilon_D^{3/4}}{\nu_g^{1/4}} \tag{31}$$

This equation, after proper transformations, takes the form:

$$\beta_{tk}(d_1, d_2) = 0.0792 \frac{\rho_s}{\rho_g(x)} \frac{\varepsilon_D(x)^{3/4}}{\nu_g(x)^{5/4}} (d_1 + d_2)^2 \left| d_1^2 - d_2^2 \right| \tag{32}$$

where  $\rho_g(x)$  is the gas density and  $\nu_g(x)$  is the gas kinematic viscosity:

$$\nu_g(x) = \eta_g(x) / \rho_g(x) \tag{33}$$

and  $\varepsilon_D(x)$  is the turbulent kinetic energy (TKE) dissipation rate ( $\text{m}^3/\text{s}^2$ ).

#### 2.4.3. Turbulent–Diffusion Coagulation

The turbulent–diffusion coagulation mechanism can be also important in the turbulent flow field. The essence of this mechanism lies in the fact that particles are completely involved into turbulent motion and their collision frequency is then determined using the intensity of turbulent mixing. In this case, the coagulation kernel can be determined using the following equation suggested in [26,27]:

$$\beta_{td}(d_1, d_2) = \frac{\pi}{4} (d_1 + d_2)^2 \sqrt{\frac{8}{3\pi} \langle w^2 \rangle} \tag{34}$$

where  $\langle w^2 \rangle$  is the mean value of the squared relative velocity of interacting particles in the turbulent flow:

$$\langle w^2 \rangle = \langle u_1^2 \rangle + \langle u_2^2 \rangle - 2\psi\sqrt{\langle u_1^2 \rangle}\sqrt{\langle u_2^2 \rangle} + \frac{\psi}{12}(d_1 + d_2)^2 \frac{\varepsilon_D(x)}{\nu_g(x)} \tag{35}$$

$\psi$  is the function taking into account the velocity correlation of interacting particles;  $\langle u_1^2 \rangle$  and  $\langle u_2^2 \rangle$  are the mean values of squared particle velocities in the turbulent flow;

$$\psi = 1 - \exp\left(-\frac{\gamma_1\gamma_2}{\gamma_1 + \gamma_2}\right) \tag{36}$$

and  $\gamma_1$  and  $\gamma_2$  are the ratios of the characteristic time of small-scale turbulent pulsations to the characteristic relaxation time of particle velocity  $\tau_1$  and  $\tau_2$ , respectively:

$$\gamma_1 = \frac{1}{\tau_1} \left( \frac{\nu_g(x)}{\varepsilon_D(x)} \right)^{1/2}, \quad \gamma_2 = \frac{1}{\tau_2} \left( \frac{\nu_g(x)}{\varepsilon_D(x)} \right)^{1/2} \tag{37}$$

$$\tau_1 = \frac{1}{18} \frac{\rho_s}{\rho_g(x)} \frac{d_1^2}{\nu_g(x)}, \quad \tau_2 = \frac{1}{18} \frac{\rho_s}{\rho_g(x)} \frac{d_2^2}{\nu_g(x)} \tag{38}$$

$$\langle u_1^2 \rangle = 3.9(1 - e^{-\gamma_1})\tau_1^2 \left(1 - \frac{\rho_g(x)}{\rho_s}\right)^2 \frac{\varepsilon_D(x)^{3/2}}{\nu_g(x)^{1/2}} + \varepsilon_D(x)\tau_1 e^{-\gamma_1} \tag{39}$$

$$\langle u_2^2 \rangle = 3.9(1 - e^{-\gamma_2})\tau_2^2 \left(1 - \frac{\rho_g(x)}{\rho_s}\right)^2 \frac{\varepsilon_D(x)^{3/2}}{\nu_g(x)^{1/2}} + \varepsilon_D(x)\tau_2 e^{-\gamma_2} \tag{40}$$

The set of governing Equations (17)–(40) is supplemented with a database of thermo-physical properties of substances and integrated numerically on a given flow field in the exhaust system of an automobile diesel engine.

### 3. Results

#### 3.1. Soot Number Density and Mean Diameter in the Engine Cylinder

The developed database of Section 2.3 was used in the 3D calculation of the operation process in a diesel engine. Figure 7 shows the predicted snapshots of soot mass fraction (SMF), temperature ( $T$ ), soot-particle number density ( $n_\Sigma$ ), and soot-particle mean diameter ( $\bar{d}$ ) in the engine cylinder at different crank angles: from 720° CA to 860° CA. Soot is seen to form in the spray region at high temperatures exceeding 1400 K. Parameters  $n_\Sigma$  and  $\bar{d}$  are represented using smooth functions reasonably correlating with the SMF and temperature distributions.

Based on the distributions of  $n_\Sigma$ ,  $\bar{d}$ , and  $\sigma$  (not shown in Figure 7), one can reconstruct the temporal evolution of the local instantaneous soot-particle log-normal SDF in each point of the ICE cylinder, including the vicinity of the exhaust valve. The maximum local number density of soot particles ( $n_\Sigma \approx 10^{19} \text{ m}^{-3}$ ) is observed at  $\varphi = 726^\circ \text{ CA}$  in the spray region of the ICE cylinder. The maximum mean diameter of soot particles is  $\bar{d} = 2\text{--}3 \text{ nm}$  by this time. The maximum mean diameter of soot particles in this example ( $\bar{d} \approx 11 \text{ nm}$  at  $n_\Sigma \approx 10^{18} \text{ m}^{-3}$ ) is attained at  $\varphi \approx 726^\circ \text{ CA}$  in the piston cavity in the vicinity of the wall, which is caused by a large enrichment of the mixture with fuel in this region of the cylinder. Over time, the mean diameter of soot particles in the engine cylinder reaches the level of 5–6 nm, while the number density of soot particles is on the order of  $n_\Sigma \approx 10^{17} - 10^{18} \text{ m}^{-3}$ .

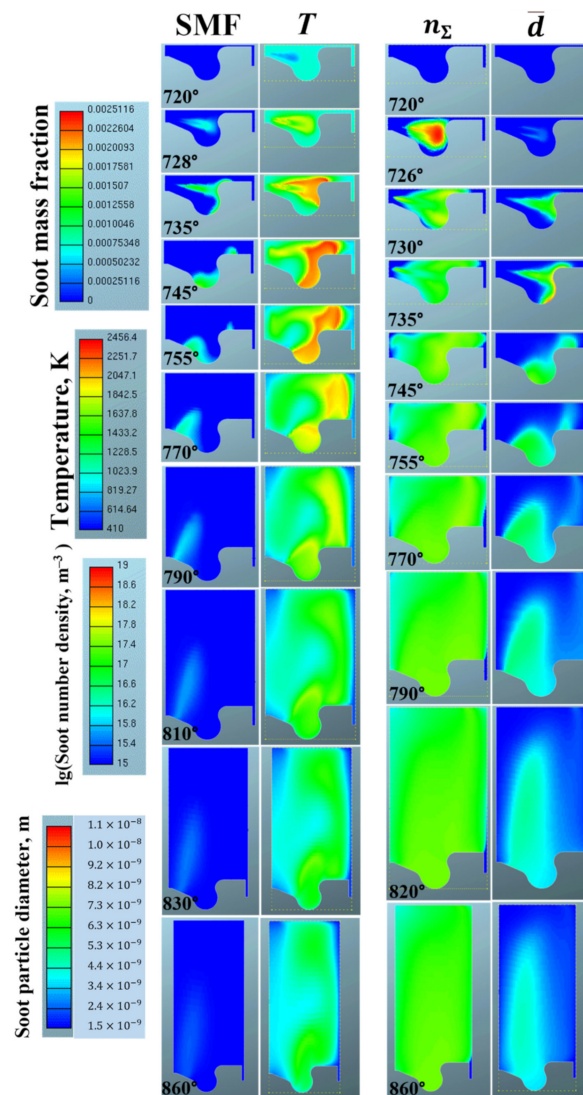


**Figure 7.** Snapshots of soot mass fraction, temperature, soot particle number density, and mean diameter at different crank angles.

### 3.2. Soot Particle Coagulation in the Engine Exhaust System

Figure 8 shows the calculated 3D fields of flow velocity (Figure 8a), TKE dissipation rate (Figure 8b), absolute pressure (Figure 8c), and temperature (Figure 8d) at a time of 80 s after the start of manifold operation. The following boundary conditions were at the inlet: flow rate 0.05 kg/s; temperature 600 K; and at the outlet: pressure 101,000 Pa. Figure 9a,b show the cross-section averaged longitudinal distributions of the gas velocity and the turbulent kinetic energy dissipation.

Two independent algorithms were used to solve the problem: an algorithm with a static particle size grid and an algorithm with an adaptive dynamic grid. In both algorithms, a discrete analogue of the initial log-normal particle SDF was first formed, and then the set of Equations (18)–(40) was solved using conservative difference methods. Both algorithms led to the same results. Figure 10a shows an example of coagulation simulation along the diesel exhaust system at  $n_{\Sigma, \text{in}} = 2 \cdot 10^{18} \text{ m}^{-3}$ ,  $\bar{d}_{\text{in}} = 10 \text{ nm}$ , and  $\sigma_{\text{in}} = 0.38$ . These values approximately correspond to the mean values of  $n_{\Sigma, \text{in}}$ ,  $\bar{d}_{\text{in}}$ , and  $\sigma_{\text{in}}$  during the entire period of the engine exhaust process. Note that Figure 10a shows the particle volume-based SDF, which is proportional to the total volume occupied by soot particles rather than to their total number density. It follows from Figure 10a that the volume-based SDF undergoes a significant transformation: the mean particle diameter changes from  $\bar{d}_{\text{in}} = 10 \text{ nm}$  at the inlet

to the exhaust system to  $\overline{d_{out}} \approx 85$  nm at its outlet. Interestingly, the particle coagulation process mostly occurs in the first half of the exhaust pipe, whereas in its second part, the transformation of the SDF is considerably less pronounced. In this example, among the three coagulation mechanisms considered, the Brownian mechanism turned out to be dominant, while both turbulent mechanisms had almost no effect on the evolution of the soot-particle SDF. When the mean particle diameter at the inlet of the exhaust system,  $\overline{d_{in}}$ , was artificially changed from 10 to 60 nm (*ceteris paribus*), the mean particle diameter at the system outlet,  $\overline{d_{out}}$ , changed almost linearly (Figure 10b) and attained  $\overline{d_{out}} \approx 510$  nm. Additional analysis showed that the shape of the volume-based SDF during coagulation remained log-normal.

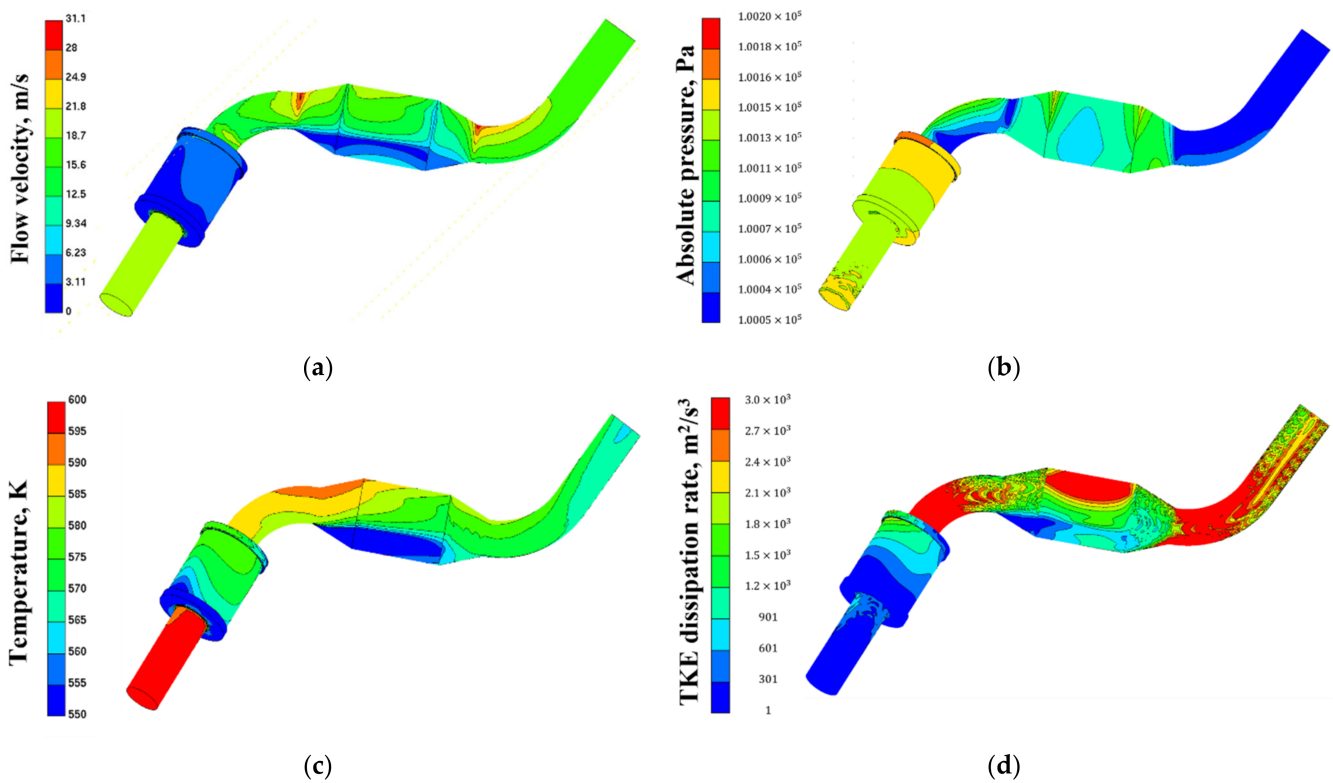


Figure 8. Calculated 3D flow fields in the engine exhaust system at  $t = 80$  s: (a) flow velocity, (b) absolute pressure, (c) temperature, and (d) TKE dissipation rate.

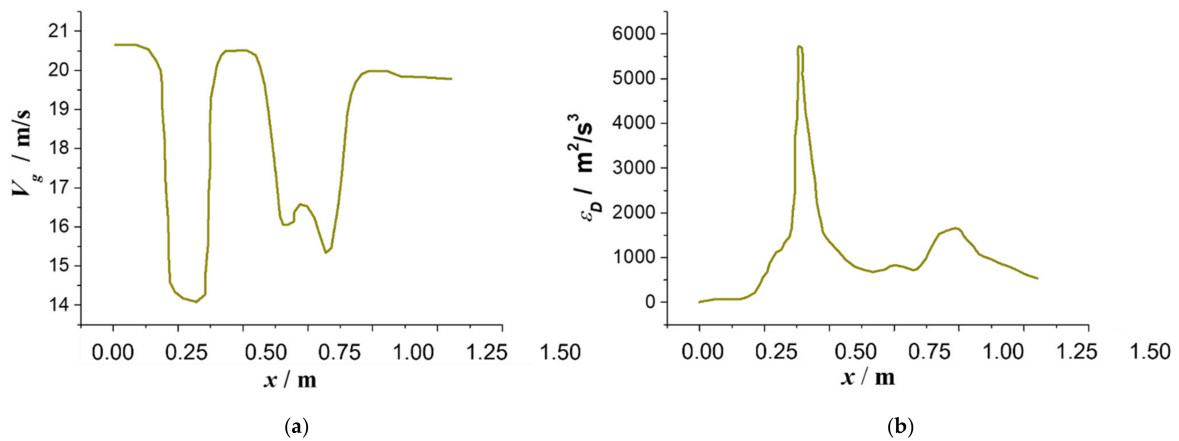
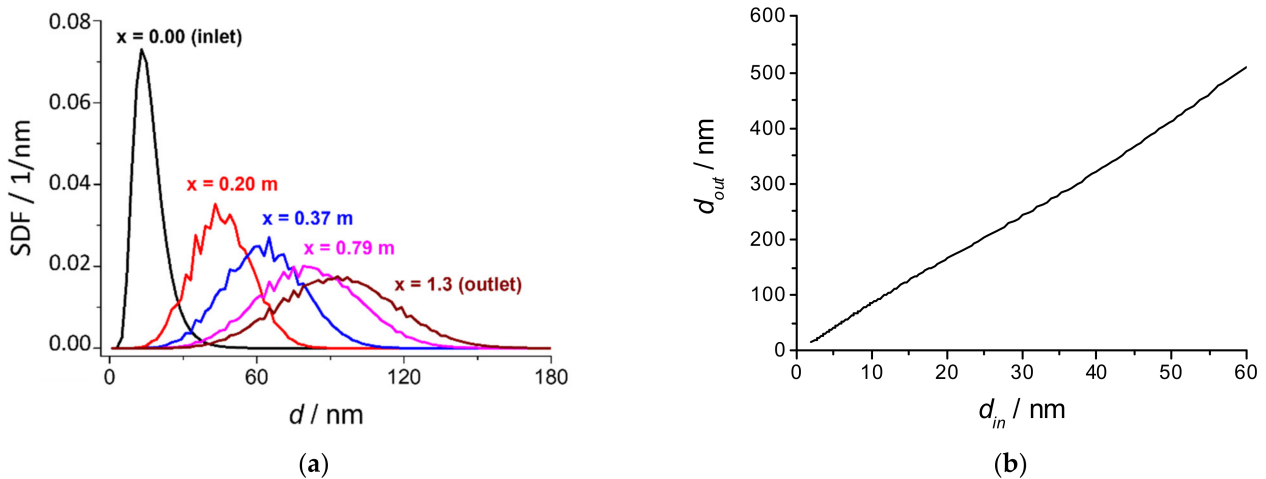
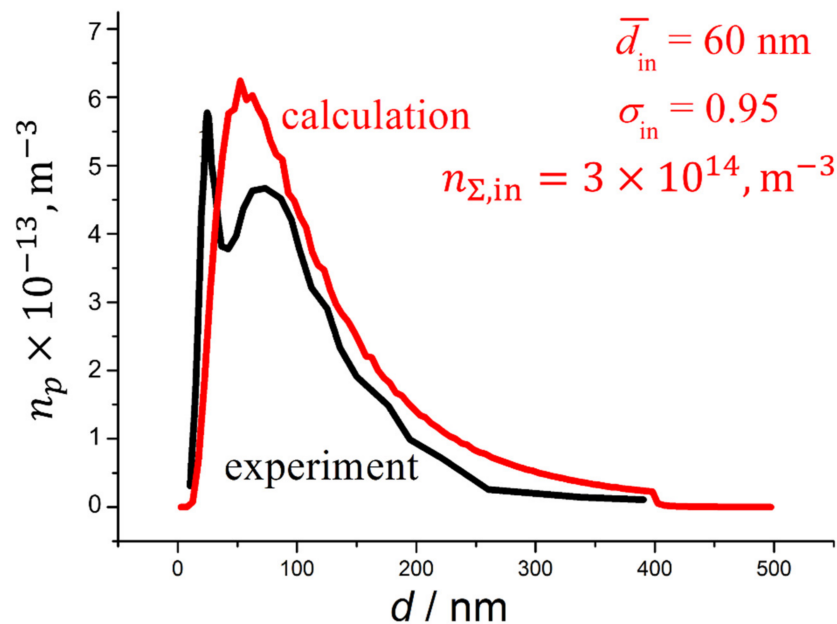


Figure 9. Cross-section-averaged distributions of (a) gas velocity and (b) TKE dissipation rate along the exhaust pipe.



**Figure 10.** (a) Temporal evolution of the soot-particle SDF along the exhaust system of a diesel engine and (b) the dependence of the mean diameter of soot particles in the outlet section of the exhaust system on the mean particle diameter in the inlet section.

Figure 11 compares the calculated and measured [37] dependences of soot particle number concentration,  $n_p$ , on particle diameter. The experimental curve is constructed based on the results of measurements at the outlet of the exhaust system of a real large-size diesel engine [37]. In the experiment, the mean particle size  $\bar{d}_{out}$  was about 140 nm. The calculated log-normal SDF was obtained for such values of  $n_{\Sigma,in}$ ,  $\bar{d}_{in}$ , and  $\sigma_{in}$  at which the best agreement with the experiment was achieved. It follows from such a comparison that, taking into account the coagulation of particles in the exhaust system, their mean diameter in the diesel cylinder should be at a level of  $\bar{d}_{in} \approx 60$  nm. This important conclusion should be kept in mind when comparing the results of calculations of soot formation in a diesel cylinder with experimental data: particle size measurements at the outlet of the exhaust system may have nothing to do with particle sizes in the engine cylinder.



**Figure 11.** Comparison of measured [37] and simulated particle number concentrations at the outlet of the engine exhaust system. The values of  $\bar{d}_{in}$ ,  $\sigma_{in}$ , and  $n_{\Sigma,in}$  are obtained by solving the inverse problem.

#### 4. Discussion

The computational approach and the tool allowing for simulating the soot-particle SDF at the entrance to the ICE exhaust pipe and further temporal evolution of this SDF due to particle coagulation involving Brownian, turbulent-kinetic, and turbulent-diffusion mechanism has been developed and tested. The tool contains two blocks. The first block is the database of look-up tables for reconstructing the temporal evolution of the local instantaneous soot-particle log-normal SDF in either location of the ICE cylinder based on the time-dependent parameters  $n_{\Sigma}(t)$ ,  $\bar{d}(t)$ , and  $\sigma(t)$  with a discrete set of time from 0 to 3 ms. This database is developed using detailed calculations of soot formation during pyrolysis and oxidation of the various hydrocarbons behind reflected shock waves in a kinetic shock tube. The list of hydrocarbons currently includes  $\text{CH}_4$ ,  $\text{C}_2\text{H}_5\text{OH}$ ,  $\text{C}_3\text{H}_8$ ,  $\text{n-C}_7\text{H}_{16}$ ,  $\text{i-C}_8\text{H}_{18}$ ,  $\text{n-C}_{10}\text{H}_{22}$ , and  $\text{n-C}_{14}\text{H}_{30}$ , and can be readily extended. The second block is the code-solving Equation (18) on the given 1D flow field in the ICE exhaust system. The 1D flow field is obtained by averaging the 3D CFD solution over the cross-section of the exhaust pipe. The source term in Equation (7) includes Brownian, turbulent-kinetic, and turbulent-diffusion mechanisms of soot particle coagulation. The boundary condition for the soot-particle SDF at the inlet of the exhaust pipe for Equation (18) is taken from the CFD solution of the ICE operation process in the form of the local instantaneous soot-particle log-normal SDF in the vicinity of the open exhaust valve. The application of the tool is demonstrated using the example of a diesel engine operating on n-tetradecane as a surrogate of diesel oil. The results of this particular calculation indicate that most soot forms in the fuel-rich spray region after ignition, whereas the mean soot particle diameter is about several nanometers. Thereafter, the mean diameter of soot particles varies with time and position attaining the maximum value of about 10 nm, which gradually decreases with time due to soot oxidation. Coagulation of soot particles in the engine exhaust pipe results in drastic transformations of the SDF. In the exhaust pipe, the mean particle diameter increases by about an order of magnitude (from 10 to 85 nm). The particle coagulation process mostly occurs in the first half of the exhaust pipe, whereas in its second part, the transformation of the SDF is considerably less pronounced. Among the three coagulation mechanisms considered, the Brownian mechanism turned out to be dominant, while both turbulent mechanisms had almost no effect on the evolution of the soot-particle SDF. The suggested computational approach was used for solving an inverse problem of determining the soot-particle SDF in the engine cylinder based on the measured dependence of the soot-particle number concentration vs. particle diameter obtained experimentally at the exit of the exhaust pipe of a large-scale diesel engine [37]. It appeared that the estimated mean diameter of soot particles entering the engine exhaust pipe was a factor of 2.3 less than that measured at the pipe exit. This important conclusion should be kept in mind when comparing the results of simulations of soot formation in a diesel cylinder with experimental data: particle size measurements at the outlet of the exhaust system may have nothing in common with particle sizes in the engine cylinder.

#### 5. Conclusions

Thus, a unique database for simulating the size distribution functions of soot particles in ICEs has been developed. The database is formatted as look-up tables and can be used in multidimensional calculations of the engine operation process. This manuscript presents a brief description of the database and an example of its application in the 3D calculation of the diesel engine operation process.

A model for the coagulation of soot particles in the exhaust system of a reciprocating engine has been proposed, which includes three mechanisms: Brownian, turbulent-diffusion, and turbulent-kinetic. Calculations have shown that the coagulation process has a significant effect on the mean size of soot particles in the outlet section of the exhaust system (the average diameter can increase by almost an order of magnitude), and the dominant mechanism of particle coagulation in the exhaust system of a diesel engine is the Brownian mechanism.

Further model development will be focused on the refinement of the database of soot-particle parameters. Importantly, the detailed model of soot formation underlying the current database was validated against the available experimental data on the soot yield during pyrolysis and partial oxidation of various hydrocarbons obtained in kinetic shock tubes rather than in internal combustion engines. The conditions behind reflected shock waves can differ considerably from those in engines.

**Author Contributions:** Conceptualization, S.M.F.; methodology, S.M.F.; investigation, K.A.A., V.S.I., P.A.V., F.S.F., I.V.S. and M.S.B.; data curation, K.A.A., V.S.I., P.A.V. and F.S.F.; formal analysis—I.V.S. and M.S.B.; writing—original draft preparation, S.M.F.; writing—review and editing, S.M.F.; supervision, S.M.F.; project administration, S.M.F.; funding acquisition, S.M.F. All authors have read and agreed to the published version of the manuscript.

**Funding:** This research was supported by a subsidy given to the Federal State Institution “Scientific Research Institute for System Analysis of the Russian Academy of Sciences” to implement the state assignment on the topic No. FNEF-2022-0005 (Registration No. 1021060708369-1-1.2.1).

**Institutional Review Board Statement:** Not applicable.

**Informed Consent Statement:** Not applicable.

**Data Availability Statement:** Not applicable.

**Conflicts of Interest:** The authors declare no conflict of interest.

### Abbreviations

AFM	Atomic force microscopy
AMG	Algebraic multi-grid
CA	Crank angle
CG	Conjugate gradient
DMS	Detailed model of soot formation
EGR	Exhaust Gas Recirculation
HACA	H-abstraction-Acetylene-addition
ICE	Internal combustion engine
PAH	Polycyclic aromatic hydrocarbons
RANS	Reynolds-averaged Navier–Stokes
SDF	Size distribution function
SIMPLE	Semi-Implicit Method for Pressure Linked Equations
SMF	Soot mass fraction
TKE	Turbulent kinetic energy

### Appendix A. Kinetic Soot Model in AVL FIRE

The basis of the kinetic soot model is a detailed chemical reaction scheme for the calculation of soot formation and oxidation. The complete detailed kinetic scheme of the soot formation process incorporates 1850 gas-phase reactions, 186 species, and 100 heterogeneous reactions with the participation of 4 ensembles of micro-heterogeneous particles of different types. The current model contains a reduced number of species and reactions and has been developed in order to provide a computationally efficient kinetic overall soot model. The model can describe the behavior of soot formation and oxidation for different fuel classes. Exact reaction constants have been implemented for methane, propane, ethanol, n-heptane, iso-octane, n-decane, and n-tetradecane. If the fuel which has been specified by the user does not exactly match one of these species, AVL FIRE chooses automatically the best parameter set to be used.

## References

1. Commission Regulation (EC) No 692/2008 of 18 July 2008. p. 130. Available online: [http://ec.europa.eu/enterprise/sectors/automotive/environment/eurovi/index\\_en.htm](http://ec.europa.eu/enterprise/sectors/automotive/environment/eurovi/index_en.htm) (accessed on 15 May 2022).
2. Hiroyasu, H.; Kadota, T. Models for Combustion and Formation of Nitric Oxide and Soot in Direct Injection Diesel Engines. *SAE Techn. Paper* **1976**, 760129. [[CrossRef](#)]
3. Payri, R.; García-Oliver, J.M.; Bardi, M.; Manin, J. Fuel temperature influence on diesel sprays in inert and reacting conditions. *Appl. Therm. Eng.* **2012**, *35*, 185–195. [[CrossRef](#)]
4. Nishida, K.; Zhu, J.; Leng, X.; He, Z. Effects of micro-hole nozzle and ultra-high injection pressure on air entrainment, liquid penetration, flame lift-off and soot formation of diesel spray flame. *Int. J. Engine Res.* **2017**, *18*, 51–65. [[CrossRef](#)]
5. Samir Chandra Ray, S.; Keiya Nishida, K.; McDonell, V.; Ogata, Y. Effects of full transient injection rate and initial spray trajectory angle profiles on the CFD simulation of evaporating diesel sprays—Comparison between single-hole and multihole injectors. *Energy* **2023**, *263*, 125796. [[CrossRef](#)]
6. Agafonov, G.L.; Nullmeier, M.; Vlasov, P.A.; Warnatz, J.; Zaslono, I.S. Kinetic Modeling of Solid Carbon Particle Formation and Thermal Decomposition during Carbon Suboxide Pyrolysis behind Shock Waves. *Combust. Sci. Techn.* **2002**, *174*, 185–213. [[CrossRef](#)]
7. Agafonov, G.L.; Smirnov, V.N.; Vlasov, P.A. Shock tube and modeling study of soot formation during the pyrolysis and oxidation of a number of aliphatic and aromatic hydrocarbons. *Proc. Combust. Inst.* **2011**, *33*, 625–632. [[CrossRef](#)]
8. Basevich, V.Y.; Vlasov, P.A.; Skripnik, A.A.; Frolov, S.M. Modeling of soot formation in internal combustion engines. *Combust. Explos.* **2008**, *1*, 40–43.
9. Appel, J.; Bockhorn, H.; Frenklach, M. Kinetic Modeling of soot formation with detailed chemistry and physics: Laminar premixed flames of C2 hydrocarbons. *Combust. Flame* **2000**, *121*, 122–136. [[CrossRef](#)]
10. Evlampiev, A.V.; Frolov, S.M.; Basevich, V.Y.; Belyaev, A.A. Overall kinetic mechanisms for modeling turbulent reactive flows. Part IV: Diffusion combustion. *Chem. Phys. Rep.* **2001**, *20*, 21–27.
11. Kiefer, J.H.; Sidhu, S.S.; Kern, R.D.; Xie, K.; Chen, H.; Harding, L.B. The homogeneous pyrolysis of acetylene II: The high temperature radical chain mechanism. *Combust. Sci. Techn.* **1992**, *82*, 101–130. [[CrossRef](#)]
12. Krestinin, A.V. Detailed modeling of soot formation in hydrocarbon pyrolysis. *Combust. Flame* **2000**, *121*, 513–524. [[CrossRef](#)]
13. Wagner, H.G.; Vlasov, P.A.; Dörge, K.J.; Eremin, A.V.; Zaslono, I.S.; Tanke, D. The kinetics of carbon cluster formation during C3O2 pyrolysis. *Kinet. Catal.* **2001**, *42*, 645–656. [[CrossRef](#)]
14. Wang, H.; Frenklach, M. A Detailed kinetic modeling study of aromatics formation in laminar premixed acetylene and ethylene flames. *Combust. Flame* **1997**, *110*, 173–221. [[CrossRef](#)]
15. Frenklach, M.; Mebel, A. On the mechanism of soot nucleation. *Phys. Chem. Chem. Phys.* **2020**, *22*, 5314–5331. [[CrossRef](#)] [[PubMed](#)]
16. Frenklach, M.; Clary, D.W.; Gardiner, W.C., Jr.; Stein, S.E. Detailed kinetic modeling of soot formation in shock-tube pyrolysis of acetylene. *Proc. Combust. Inst.* **1985**, *20*, 887–901. [[CrossRef](#)]
17. Commodo, M.; Kaiser, K.; De Falco, G.; Minutolo, P.; Schulz, F.; D’Anna, A.; Gross, L. On the early stages of soot formation: Molecular structure elucidation by high-resolution atomic force microscopy. *Combust. Flame* **2019**, *205*, 154–164. [[CrossRef](#)]
18. Schulz, F.; Commodo, M.; Kaiser, K.; De Falco, G.; Minutolo, P.; Meyer, G.; D’Anna, A.; Gross, L. Insights into incipient soot formation by atomic force microscopy. *Proc. Combust. Inst.* **2019**, *37*, 885–892. [[CrossRef](#)]
19. Botero, M.L.; Sheng, Y.; Akroyd, J.; Martin, J.; Dreyer, J.A.H.; Yang, W.; Kraft, M. Internal structure of soot particles in a diffusion flame. *Carbon* **2019**, *141*, 635–642. [[CrossRef](#)]
20. Irimiea, C.; Faccinetto, A.; Mercier, X.; Ortega, I.-K.; Nuns, N.; Therssen, E.; Desgroux, P.; Focsa, C. Unveiling trends in soot nucleation and growth: When secondary ion mass spectrometry meets statistical analysis. *Carbon* **2019**, *144*, 815–830. [[CrossRef](#)]
21. Mitra, T.; Zhang, T.; Sediako, A.D.; Thomson, M.J. Understanding the formation and growth of polycyclic aromatic hydrocarbons (PAHs) and young soot from n-dodecane in a sooting laminar coflow diffusion flame. *Combust. Flame* **2019**, *202*, 33–42. [[CrossRef](#)]
22. Hou, D.; Lindberg, C.S.; Manuputty, M.Y.; You, X.; Kraft, M. Modelling soot formation in a benchmark ethylene stagnation flame with a new detailed population balance model. *Combust. Flame* **2019**, *203*, 56–71. [[CrossRef](#)]
23. Payne, J.F.B.; Skyrme, G. An analytical means of comparing the rates of different agglomeration mechanisms, and its application to a PWR containment. *Int. J. Multiphase Flow* **1993**, *19*, 451–470. [[CrossRef](#)]
24. Friedlander, S.K. *Smoke, Dust and Haze: Fundamentals of Aerosols Dynamics*, 2nd ed.; Oxford University Press Inc.: New York, NY, USA; Oxford, UK, 2000.
25. Levich, V.G. *Physico-Chemical Hydrodynamics*; State Publ. Phys. Math. Lit.: Moscow, Russia, 1959.
26. Piskunov, V.N. *Theoretical Models of Aerosol Formation Kinetics*; Russian Federal Nuclear Center: Sarov, Russia, 2000.
27. Piskunov, V.N.; Golubev, A.I.; Goncharov, E.A.; Ismailov, N.N. Novel model of coagulation kinetics for composite particles. *Progr. Nucl. Sci. Techn. Ser. Theor. Appl. Phys.* **1996**, *3*, 12–30.
28. Frolov, S.M.; Sergeev, S.S.; Basevich, V.Y.; Frolov, F.S.; Basara, B.; Priesching, P. Simulation of multistage autoignition in diesel engine based on the detailed reaction mechanism of fuel oxidation. In *Advances in Engine and Powertrain Research and Technology. Mechanisms and Machine Science*; Parikyan, T., Ed.; Springer: Cham, Switzerland, 2022; Volume 114, pp. 149–165. [[CrossRef](#)]
29. AVL FIRE®. Computational Fluid Dynamics for Conventional and Alternative Powertrain Development. Available online: <https://www.avl.com/fire> (accessed on 26 September 2022).

30. Hanjalic, K.; Popovac, M.; Hadziabdic, M. A robust near wall elliptic relaxation eddy-viscosity turbulence model for CFD. *Int. J. Heat Fluid Flow* **2004**, *25*, 897–901. [[CrossRef](#)]
31. Rhie, C.M.; Chow, W.L. Numerical study of the turbulent flow past an airfoil with trailing edge separation. *AIAA J.* **1983**, *21*, 1525. [[CrossRef](#)]
32. Przulj, V.; Basara, B. Bounded convection schemes for unstructured grids. In Proceedings of the 15th AIAA Computational Fluid Dynamics Conference, Anaheim, CA, USA, 11–14 June 2001. AIAA paper 2001-2593.
33. Marthur, S.R.; Murthy, J.Y. A pressure-based method for unstructured meshes. *Numer. Heat Transfer B* **1997**, *31*, 195–215. [[CrossRef](#)]
34. Muzaferija, S. Adaptive Finite Volume Method for Flow Predictions using Unstructured Meshes and Multigrid Approach. Ph.D. Thesis, University of London, London, UK, 1994.
35. Emans, M. Performance of parallel AMG-precoditiones on CFD-codes for weakly compressible flows. *Parallel Comput.* **2010**, *36*, 326–338. [[CrossRef](#)]
36. Patankar, S.V.; Spalding, D.B. A calculation procedure for heat, mass and momentum transfer in three-dimensional parabolic flows. *Int. J. Heat Mass Transfer* **1972**, *15*, 1510–1520. [[CrossRef](#)]
37. Petrovich, V. Methods for measurement and verification of ultra fine particles concentration from diesel engine emission. In Proceedings of the International Automotive Conference “Science and Motor Vehicles 2011”, Belgrad, Serbia, 19–21 April 2011. paper #NMMV11-5E03.

**Disclaimer/Publisher’s Note:** The statements, opinions and data contained in all publications are solely those of the individual author(s) and contributor(s) and not of MDPI and/or the editor(s). MDPI and/or the editor(s) disclaim responsibility for any injury to people or property resulting from any ideas, methods, instructions or products referred to in the content.